Effect of scattering and contacts on current and electrostatics in carbon nanotubes

A. Svizhenko* and M. P. Anantram†
Center for Nanotechnology and NASA Advanced Supercomputing Division, NASA Ames Research Center, Mail Stop: 229-1 Moffett Field, California 94035-1000, USA
(Received 23 December 2004; published 12 August 2005)

We computationally study the electrostatic potential profile and current carrying capacity of carbon nanotubes as a function of length and diameter. Our study is based on solving the nonequilibrium Green's function and Poisson equations self-consistently, including the effect of electron-phonon scattering. A transition from the ballistic to diffusive regime of electron transport with an increase of applied bias is manifested by qualitative changes in the potential profiles, differential conductance, and electric field in a nanotube. In the low-bias ballistic limit, most of the applied voltage drop occurs near the contacts. In addition, the electric field at the tube center increases proportionally with diameter. In contrast, at high biases, most of the applied voltage drops across the nanotube, and the electric field at the tube center decreases with an increase in diameter. We find that the differential conductance can increase or decrease with bias as a result of an interplay of nanotube length, diameter, and a quality factor of the contacts. From an application viewpoint, we find that the current carrying capacity of nanotubes increases with an increase in diameter. Finally, we investigate the role of inner tubes in affecting the current carried by the outermost tube of a multiwalled nanotube.

DOI: 10.1103/PhysRevB.72.085430 PACS number(s): 72.10.−d, 73.23.Ad, 73.63.Fg, 73.63.Nm

I. INTRODUCTION

Metallic carbon nanotubes are near-ideal conductors of current.[1–5] While a single nanotube can be used as an interconnect in molecular electronics, nanotube arrays have shown promise as more conventional interconnects in conjunction with silicon technology.[6,7] A single nanotube has two modes that carry current at the Fermi energy, which yields a low-bias conductance of $4e^2/h$ and resistance of 6.5 kΩ. This corresponds to a current of 155 μA at a bias of 1 V. Noting that a nanotube diameter can be as small as 5 Å, it is easy to estimate that an array of metallic carbon nanotubes can carry current densities larger than 10^{10} A/cm^2. In fact, current densities approaching 10^9 A/cm^2 have been demonstrated.[3,8]

The diameter of both metallic and semiconducting nanotubes can vary from 5 Å to many tens of nanometers, with the electronic properties determined by the chiral angle. The band gap of semiconducting nanotubes decreases inversely with diameter. As a result, a large-diameter nanotube with a diameter of 19 nm will have a half band gap of less than 2.5 kT at room temperature, meaning that large-diameter semiconducting nanotubes carry non-negligible current. Further, electrical contact can be made to many shells of large-diameter multiwalled carbon nanotubes. Reference 3 demonstrated a resistance of nearly 500 Ω in a multiwalled sample, which corresponds to about 12 conducting shells. Therefore, both small- and large-diameter nanotubes are promising as interconnects. Experiments on small-diameter carbon nanotubes show that the differential conductance decreases with applied bias, for voltages larger than 150 mV.[9–11] Reference 9 showed that the conductance decrease with an increase in bias was caused by reflection of electrons incident in crossing subbands due to scattering with zone-boundary phonons. The noncrossing subbands of small-diameter nanotubes do not carry current due to their large band gap. In contrast, large-diameter nanotubes experimentally show an increase in conductance with applied bias.[1,2,12,13] Reference 14 suggested that as the diameter increases, electrons may tunnel into noncrossing subbands, thus causing an increase in differential conductance with applied bias. The main drawbacks of the calculation in Ref. 14 was that the results depended on the assumed form of potential drop in metallic nanotubes and, further, electron-phonon scattering was neglected. Recently, we performed self-consistent calculations,[15] which showed a dramatic increase in the differential conductance of large-diameter nanotubes with bias, in the ballistic limit. In the current work, we present results for the current flow and potential profile in metallic nanotubes from a more comprehensive model, which includes both *charge self-consistency* and *electron-phonon scattering*. The potential and current-voltage characteristics are studied as a function of nanotube diameter and length. We are primarily interested in short ($\sim$100 nm) rather than long nanotubes, where the physics is more interesting and technological applications are promising. The nature of the metallic contacts is also important. From an experimental view point the contact between a metal and a nanotube can either be an end contact or side contact. The end contact corresponds to only the nanotube tip electronically interacting with the metal contact. In experiments, the end contacts usually involve strong chemical modification of the nanotube at the metal-nanotube interface.[5] Also, Ref. 1 found that end contacts without sufficient chemical modification of the nanotube-metal interface have a large contact resistance. Due to the uncertainty of the contact band structure, modeling experimental end contacts even remotely correct is difficult. The side contacts correspond to coupling between metal and nanotube atoms over many unit cells of the nanotube and can be thought of as a nanotube buried inside a metal. Most experimental configurations correspond to side contacts.[1,16] An important feature of the side contact is that the coupling between atoms in the nanotube is much stronger than coupling between nanotube

 ©2005 The American Physical Society

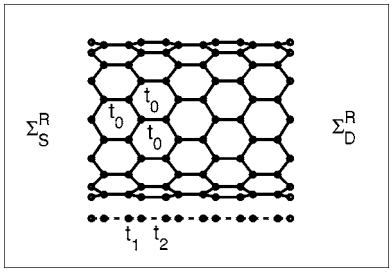


FIG. 1. Zigzag carbon nanotube and the corresponding 1D chain in mode space. The hopping parameter between nearest neighbors in the nanotube is t_0. The 1D chain has two sites per unit cell with on-site potential U_o and hopping parameters $t_1=2t_0\cos(q\pi/N)$ and $t_2=t_0$, where q represents a quantum number of the mode.

and metal atoms. In the side-contact geometry, electrons are predominantly injected from the metal into the nanotube buried in metal and then transmitted to the nanotube region between contacts. In fact, as proof of such a process, scaling of conductance with contact area has been observed in the side-contacted geometry in Refs. 1 and 16. Modeling has also shown that the conductance in metallic zigzag nanotubes can be close to the theoretical maximum of $4e^2/h$, when there is sufficient overlap with the contact.[17] In this work, we consider the metal-nanotube contact in both the limiting cases of side and end contacts.

The outline of the paper is as follows. In Sec. II, we describe the formalism. The electrostatics at low bias is presented in Sec. III A, and electrostatics at high bias and current-voltage characteristics are presented in Sec. III B, both for side contacts. The role of inner shells in affecting the potential profile of a current carrying outer shell is described in Sec. III C. End contacts that form both good and bad contacts are discussed in Sec. III D. We present our conclusions in Sec. IV.

II. FORMALISM

In this paper we consider only zigzag carbon nanotubes. The analysis for armchair nanotubes is similar. The general form of the Hamiltonian for electrons in a carbon nanotube can be written as

$$H=\sum_{i,x}U_x^i c_{i,x}^\dagger c_{i,x}+\sum_{i,j,x,x'}t_{x,x'}^{i,j}c_{i,x}^\dagger c_{j,x'}. \tag{1}$$

The sum is taken over all rings i,j in the transport direction and all atomic locations x,x' in a ring.

We make the following common approximations: (i) only nearest neighbors are included; each atom in an sp^2-coordinated carbon nanotube has three nearest neighbors, located $a_{cc}=1.42$ Å away; (ii) the band structure consists of only a π orbital, with the hopping parameter $t_0=V_{pp\pi}=-2.77$ eV and the on-site potential $U_o=\epsilon_p=0$. Such a tight-binding model is adequate to model transport properties in undeformed nanotubes. Within these approximations, only the following parameters are nonzero (see Fig. 1):

$$U_x^i=U_o,\quad \forall\, i,$$

$$t_{x,x'}^{i,i-1}=t_{x,x'}^{i-1,i}=t_0\delta_{x\pm a/2,x'},\quad \forall\, i=2k,$$

$$t_{x,x'}^{i,i+1}=t_{x,x'}^{i+1,i}=t_0\delta_{x,x'},\quad \forall\, i=2k, \tag{2}$$

where $a=a_{cc}\sqrt{3}$, integer k runs from 1 to $N_y/2$, and N_y is the total number of rings. In $(N,0)$ zigzag nanotubes, the wave vector in the circumferential direction is quantized as $\tilde{q}=2\pi q/Na$, $q=1,2,\ldots,N$, creating eigenmodes in the energy spectrum. By doing a Fourier expansion of $c_{i,x}^\dagger$ and $c_{i,x}$ in q space and using Eq. (2) we obtain a decoupled electron Hamiltonian in the eigenmode space:

$$H=\sum_q H^q, \tag{3}$$

$$H^q=\sum_i\left(U_q^i c_{i,q}^\dagger c_{i,q}+t_q^{i,i\pm1}c_{i,q}^\dagger c_{i\pm1,q}\right), \tag{4}$$

where

$$U_q^i=U_o,\quad \forall\, i,$$

$$t_q^{i,i-1}=t_q^{i-1,i}=2t_0\cos\left(\frac{\tilde{q}a}{2}\right)\equiv t_1,\quad \forall\, i=2k,$$

$$t_q^{i,i+1}=t_q^{i+1,i}=t_0\equiv t_2,\quad \forall\, i=2k. \tag{5}$$

The one-dimensional (1D) tight-binding Hamiltonian H^q describes a chain with two sites per unit cell with on-site potential U_o and hopping parameters t_1 and t_2 (Fig. 1). For numerical solution, the spatial grid corresponds to the rings of the nanotube, separated by $a_{CC}/2$ with a unit cell length of $3a_{CC}/2=2.13$ Å, which is half the unit cell length of a zigzag nanotube.

The subband dispersion relations are given by

$$E_q(k)=\pm|t_0|\left|1+4\cos\left(\frac{3a_{CC}k}{2}\right)\cos\left(\frac{q\pi}{N}\right)+4\cos^2\left(\frac{q\pi}{N}\right)\right|^{1/2}. \tag{6}$$

Therefore, when N is an integer of 3, there are two subbands with zero band gap and the tube is metallic. In the rest of the paper we distinguish between metallic or *crossing* subbands ($q=N/3$ and $2N/3$) and semiconducting or *noncrossing* subbands.

For each subband q we solve a system of transport equations:[18]

$$AG^{R,q}=I \tag{7}$$

$$AG^{<,>,q}=[\Sigma_{c,q}^{<,>}(E)+\Sigma_{ph,q}^{<,>}(E)]G^{A,q}, \tag{8}$$

where $A=E-H^q-V-\Sigma_{c,q}^R(E)-\Sigma_{ph,q}^R(E)$. A is a tridiagonal matrix with dimension equal to the number of rings, N_y. The electrostatic potential V is the same for all subbands. The self-energies $\Sigma_{c,q}^{R,<,>}(E)$ and $\Sigma_{ph,q}^{R,<,>}(E)$ represent the effect of contacts and scattering. I is the identity matrix.

The contacts are assumed to be reflectionless reservoirs maintained at equilibrium; i.e., they have well-defined

chemical potentials, equal to that of the metal leads: V_S in the source and V_D in the drain. Further, the nanotube and metal are assumed to have the same work function.

The contact self-energy $\Sigma^{R,<,>}_{c,q}=\Sigma^{R,<,>}_{S,q}+\Sigma^{R,<,>}_{D,q}$ has contributions due to the source and drain. The only nonzero elements of the matrices $\Sigma^{R,<,>}_{S,i,j,q}$ and $\Sigma^{R,<,>}_{D,i,j,q}$ are the first and last diagonal elements, respectively. The source-contact self-energy is found[19] using the the diagonal elements of the surface Green's function $g^S_{i,i,q}\equiv g^S_{i,q}$ of the leads, which are the solution of the following system of equations:

$$(a_1-t_2^2 g^S_{2,q}-\Sigma^R_{ph,1,1,q})g^S_{1,q}=1,$$

$$(a_2-t_1^2 g^S_{1,q}-\Sigma^R_{ph,2,2,q})g^S_{2,q}=1, \tag{9}$$

where the indices 1 and 2 stand for the two sites of the unit cell, $a_{1,2}=E-U_o-V_S$, and $\Sigma^R_{ph,i,i,q}$ $(i=1,2)$ are the diagonal elements of electron-phonon self-energies at the first two nodes near the source. The Green's function for the drain is solved for in a similar way by making the substitutions $t^S_{1,2}\rightarrow t^D_{2,1}$, $g^S_{1,2,q}\rightarrow g^D_{1,2,q}$ and taking $\Sigma^R_{ph,i,i,q}$ at the drain end. The expression for contact self-energies is then given by

$$\Sigma^R_{S,i,j,q}=t_2^2 g^S_{2,q}\,\delta_{i,1}\delta_{j,1},$$

$$\Sigma^R_{D,i,j,q}=t_1^2 g^D_{1,q}\,\delta_{i,N_y}\delta_{j,N_y},$$

$$\Sigma^<_{S,i,j,q}=-2if_S\,\mathrm{Im}[\Sigma^R_{S,q}]\delta_{i,1}\delta_{j,1},$$

$$\Sigma^<_{D,i,j,q}=-2if_D\,\mathrm{Im}[\Sigma^R_{D,q}]\delta_{i,N_y}\delta_{j,N_y},$$

$$\Sigma^>_{S,i,j,q}=2i(1-f_S)\mathrm{Im}[\Sigma^R_{S,q}]\delta_{i,1}\delta_{j,1},$$

$$\Sigma^>_{D,i,j,q}=2i(1-f_D)\mathrm{Im}[\Sigma^R_{D,q}]\delta_{i,N_y}\delta_{j,N_y}, \tag{10}$$

where $f_{S,D}$ are the Fermi factors in the source and drain leads and $\delta_{i,j}$ is the Kronecker delta.

The electron-phonon scattering is treated within the self-consistent Born approximation and assumed to be local; i.e., the self-energy matrices are diagonal. Depending on the mechanism, scattering can be elastic (acoustic phonon) or inelastic (optical and zone-boundary phonon):

$$\Sigma^{R,<,>}_{ph,q}=\Sigma^{R,<,>}_{el,q}+\Sigma^{R,<,>}_{in,q}, \tag{11}$$

$$\Sigma^{<,>}_{el,i,j,q}(E)=\delta_{i,j}\sum_{q'}D_{el,q,q'}G^{<,>,q'}_{i,j}(E), \tag{12}$$

$$\Sigma^<_{in,i,j,q}(E)=\delta_{i,j}\sum_{\nu,q'}D_{in,\nu,q,q'}[(n_B(\hbar\omega_\nu)+1)G^{<,q'}_{i,j}(E+\hbar\omega_\nu)+n_B(\hbar\omega_\nu)G^{<,q'}_{i,j}(E-\hbar\omega_\nu)], \tag{13}$$

$$\Sigma^>_{in,i,j,q}(E)=\delta_{i,j}\sum_{\nu,q'}D_{in,\nu,q,q'}[(n_B(\hbar\omega_\nu)+1)G^{>,q'}_{i,j}(E-\hbar\omega_\nu)+n_B(\hbar\omega_\nu)G^{>,q'}_{i,j}(E+\hbar\omega_\nu)], \tag{14}$$

$$\mathrm{Im}[\Sigma^R_{ph,q}(E)]=[\Sigma^>_{ph,q}-\Sigma^<_{ph,q}]/2i, \tag{15}$$

$$\mathrm{Re}[\Sigma^R_{ph,q}(E)]=\frac{1}{\pi}\mathbf{P}\int_{-\infty}^{+\infty}\frac{\mathrm{Im}[\Sigma^R_{ph,q}(E')]}{E'-E}dE'. \tag{16}$$

The matrix elements squared due to particular scattering mechanisms are chosen so as to satisfy experimentally measured values of the mean free path $\lambda_0^{el,in}$. Reference 20 reported $\lambda_0^{el}\approx 1.6$ μm and $\lambda_0^{in}\approx 10$ nm for a tube with a diameter of 1.8 nm, corresponding to a (24,0) nanotube. Inelastic scattering is due to zone-boundary and optical phonon modes with energies of 160 and 200 meV. Since matrix elements squared scale inversely with the chirality index,[21] one obtains for an $(N,0)$ nanotube

$$D_{el,in}\approx\frac{\hbar}{2\pi}\frac{1}{\mathrm{DOS}(E_F)\cdot\tau_{el,in}}=\frac{3a_{CC}t_0^2}{2\lambda_0^{el,in}}\left(\frac{24}{N}\right). \tag{17}$$

The decrease of scattering rate in a single subband with the chirality index is saturated by the eventual increase of the intersubband scattering due to the larger number of subbands. Thus, with the increase of the diameter, the mean free path of a nanotube approaches that of graphite.

Electron charge and current density n_i and J_i at each node i are found from the following equations:

$$n_i=-2i\sum_q\int_{V_{min}}^{-eV_S+10kT}G^{<,q}_{i,i}(E)\frac{dE}{2\pi}, \tag{18}$$

$$J_i=\frac{4e}{\hbar}\sum_q\int_{-eV_D-10kT}^{-eV_S+10kT}G^{<,q}_{i,i+1}(E)t^q_{i+1,i}\frac{dE}{2\pi}. \tag{19}$$

The lower limit of integration of Eq. (18) is determined by $V_{\min}=-3t_0-V_D-\Delta E_{rn}$, where ΔE_{rn} is a renormalization energy related to the real part of the electron-phonon self-energy.

We model the electrostatics of the nanotube as a system of point charges between the two contacts located at $y=y_S=0$ and $y=y_D=L$. The "perfect contacts" are modeled as parallel semi-infinite three-dimensional metal leads that are maintained at fixed source and drain potentials: V_S for $y<y_S$ and V_D for $y>y_D$. So while the self-energies due to contacts are identical to that of a semi-infinite nanotube, the role of electrostatics is included by image charges corresponding to a perfect metal. The electrostatic potential consists of a linear drop due to a uniform electric field created by the leads and the potential due to the charges on the tube and their images,

$$V=-eV_S-e(V_D-V_S)(y-y_S)/(y_D-y_S)+\sum_j\Lambda(i,j)(n_j-N), \tag{20}$$

with the electrostatic Green's function

$$\Lambda(i,j)=\frac{e}{4N\pi\epsilon_o}\sum_{n=-\infty}^{+\infty}\sum_l\left[\frac{1}{\sqrt{(y_i-y_j+2nL)^2+\rho^2_{k,l}}}-\frac{1}{\sqrt{(y_i+y_j+2nL)^2+\rho^2_{k,l}}}\right]. \tag{21}$$

Here, $\rho_{k,l}$ is the radial projection of the vector between atom k at ring i and atom l at ring j. The summation is performed

over all atoms l at ring j for an arbitrary value of k. Maintaining the nanotube atoms buried in the metal at a fixed potential is close to reality because of the screening properties of 3D metals. Within a few atomic layers from the metal surface, the potential should have approached the bulk values. One drawback of our approach is that the variation of the electrostatic potential in these few atomic layers of the 3D metal is not captured in our model. The mean-field approach of this paper neglects electron correlation effects. Since we study room-temperature, high-bias, and strong electron-phonon situations, we assume that such effects are less important.

The calculations for one bias point involve two simultaneous iterative processes: Born iterations for electron-phonon self-energies [Eqs. (7)–(16)] and Poisson iterations [Eqs. (7)–(20)] for the potential profile and charge distribution. Typically, three to five Born iterations were performed before updating a potential profile using Eq. (20). To calculate the electron charge, the solution of Eqs. (7) and (8) employs our recursive algorithm,[19] which scales linearly with the number of nodes.

Importance of self-consistency and the proper treatment of electron-phonon scattering

A major computational burden of the approach discussed above is the self-consistent procedure and the evaluation of the Kramers-Krönig relation [Eq. (16)]. In order to calculate the integral in Eq. (16), we have to solve Eqs. (7)–(15) over the whole band $[-3t_0-V_D-\Delta E_{rn};+3t_0+\Delta E_{rn}]$. Due to the presence of inelastic scattering, the energy grid has to be uniform. Equation (16) requires Ne^2Ny multiplications for each subband, which makes it very time consuming: typically, $Ne=10^4$ energy grid points are used in order to achieve a required precision in computing the charge. Such computational requirements pose a question of whether and what kind of sophistication is required in order to obtain I-V characteristics. For the case of small-diameter nanotubes, we note that a contribution to current by crossing subbands in metallic nanotubes under a moderate bias does not depend significantly on the potential profile. The reason is that the density of states of crossing subbands is nearly constant around the Fermi energy and therefore the transmission is insensitive to changes in the potential profile. It is also clear that the renormalization of subbands due to scattering affects only band edges, but does not influence the density of states of crossing subbands near the Fermi energy. These two facts allow us to conclude that neither self-consistency nor the Kramers-Krönig relation [Eq. (16)] is necessary to obtain I-V characteristics in small-diameter metallic nanotubes under a moderate bias. The criterion for this approximation is that the bias be lower than the band gap of the first noncrossing subband E_{NC1} renormalized with energy ΔE_{rn} and given by

$$E_{NC1} = 2\left[\left|t_0\right|\left|1-2\cos\left(\frac{\pi}{3}-\frac{\pi}{N}\right)\right|-\Delta E_{rn}\right] \sim 2(|t_0|\pi\sqrt{3}/N-\Delta E_{rn}), \quad \text{for large } N. \qquad (22)$$

Such an approximation, applicable, e.g., to a (12,0) nanotube under a bias smaller than 1 V, while giving incorrect potential profiles, would still result in a correct current with or without scattering.

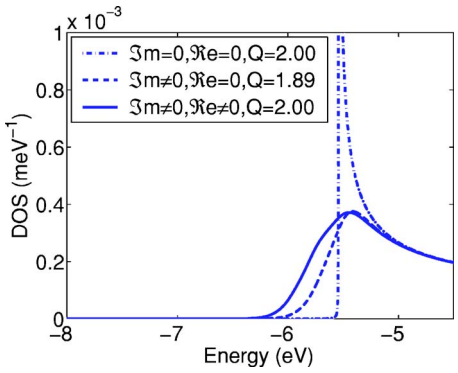


FIG. 2. (Color online) Density of states in a (12,0) nanotube under a zero bias for a fixed potential $V(y)=0$. The area under each curve, $Q=\int \mathrm{DOS}(E)dE$, gives twice the charge per subband. Including only the imaginary part of scattering self-energy (dashed) results in a loss of charge.

As will be seen later, in studying current through large-diameter nanotubes it is important to take into account the contribution to current by noncrossing subbands. Tunneling noncrossing subbands has a lower threshold bias [Eq. (22)] and depends exponentially on the slope of the potential near the edges of the tube. Therefore, a self-consistent solution for the shape of tunneling barrier is a must for large-diameter nanotubes at all biases. This, in turn, necessitates exact knowledge of the electron charge and density of states. We now discuss how much the real part of the electron-phonon retarded self-energy, $\mathrm{Re}[\Sigma^R_{ph,q}(E)]$, and thus the renormalization of the density of states affects the potential profile. In previous studies[22] $\mathrm{Re}[\Sigma^R_{ph,q}(E)]$ was set to zero, which naturally alleviates computational requirements. In Fig. 2 we show the density of states of crossing subbands versus energy in a (12,0) nanotube under zero bias. The Poisson iterations were switched off and the potential $V(y)=0$. Three curves represent different approximations to electron transport: ballistic case, when both real and imaginary parts of the electron-phonon self-energies are set to zero (dash-dotted line); scattering case, when only the imaginary part is taken into account (dashed line); and scattering case, with nonzero imaginary and real parts (solid line). For the scattering cases, transport equations were iterated for long enough to achieve convergence of electron-phonon self-energies; i.e., the self-consistent Born approximation is satisfied. The area under the ballistic curve $Q=\int \mathrm{DOS}(E)dE$ is equal to 2 which is twice the charge per subband. The important consequence of taking into account only the imaginary part of the retarded self-energy is that the area Q decreases, resulting in $\sim 5\%$ loss of electron charge. When both real and imaginary parts are taken into account, electron charge is recovered due to the shift of the subband bottom. The loss of charge when the real part is neglected results in a completely incorrect potential profile when solving transport equations self-consistently with the Poisson equation [Eq. (20)]. In Fig. 3 we show potential profiles with and without a real part of the electron-phonon self-energy when both Born and Poisson iterations

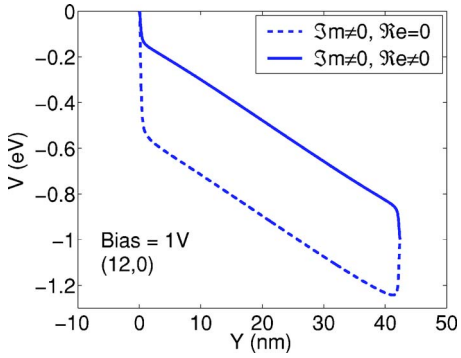


FIG. 3. (Color online) Converged potential profiles versus position for (12,0) nanotube for the cases when the real part of electron-phonon self-energy is neglected (dashed line) or taken into account (solid line). Neglecting the real part results in a severe downshift of potential profile.

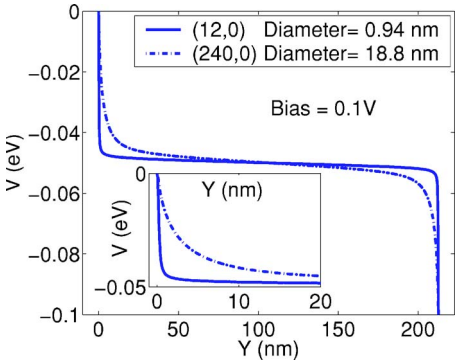


FIG. 5. (Color online) Potential versus position for (12,0) and (240,0) nanotubes, which have diameters of 0.94 and 18.8 nm, respectively. The screening for the large-diameter nanotube is significantly poorer. The inset magnifies the potential close to the nanotube-contact interface.

have converged. The applied voltage drops symmetrically across the nanotube when scattering is treated properly (solid line). When the real part is neglected, the profile shows a severe downshift due to a missing electron charge (dashed line). Such an incorrect potential profile will result in a large error in current due to the noncrossing subbands in large-diameter nanotubes. Another source of error is an overestimated band gap [Eq. (22)] and a higher threshold for the onset of current due to the noncrossing subbands. In this work, all our self-consistent calculations included Eq. (16) for the real part of the electron-phonon self-energy.

III. RESULTS

A. Electrostatics at low bias

The mean free path due to scattering with acoustic phonons is in the range of a micron.[9,20] At low biases—i.e., biases lower than the inelastic phonon energy—electron-phonon scattering does not play a significant role in determining the potential profile for tubes of moderate length (less than few hundreds of nanometer). The potential profiles for (12,0) nanotubes of lengths 21.3 and 213 nm are shown in Fig. 4. The edges of the nanotube near the contact rapidly screen the applied bias and electric field. The potential drop

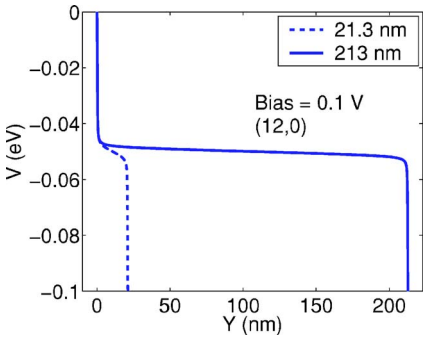


FIG. 4. (Color online) Potential versus position for (12,0) nanotubes of lengths 21.3 and 213 nm. The diameter of the (12,0) nanotube is 0.94 nm, and the applied bias is 100 mV.

is divided unequally between different parts of the nanotube, with 90% of the applied bias falling within 1 nm from the edges for both lengths. Note that had our model solved Poisson's equation in the contacts, the drop at the edges would have been smaller.

While the density of states (DOS) per unit length of metallic nanotubes is independent of diameter, the DOS per atom is inversely proportional to the diameter:

$$\mathrm{DOS}(E_F)/\mathrm{atom} = \frac{2}{t_0 N}, \tag{23}$$

where N is the number of atoms in a ring of an $(N,0)$ nanotube. As a result, we find that the screening of metallic nanotubes degrades with diameter. The potential drop for two nanotubes with diameters of 0.94 nm [(12,0) nanotube] and 18.8 nm [(240,0) nanotube] are shown in Fig. 5. Clearly, screening is poorer in the larger-diameter nanotube. In fact, while the potential drops by 45 mV in a distance of 1 nm from the edge for the (12,0) nanotube, the potential drop is only 17 mV for the (240,0) nanotube. The inset of Fig. 5 shows a substantially larger electric field away from the edges of the large-diameter nanotube.

The electric field at the center of the nanotube as a function of length is shown in Fig. 6 for the tube with a diameter of 0.94 nm. We find that for all diameters, the electric field decreases more rapidly than $1/L$, where L is the length of the nanotube. The exact power law, however, depends on the diameter. If the computed electric field versus length is fit to $1/L^a$, the exponent a increases with an increase in chirality. The value of a increases from 1.25 to 1.75 as the diameter increases from 0.94 to 18.85 nm. Similarly, the electric field versus diameter can be fit to D^b, where $0<b<1$.

B. Electrostatics at high bias and current-voltage characteristics

At biases larger than 150 mV, the main scattering mechanism in defect-free carbon nanotubes is the electron-phonon interaction. Yao, Kane, and Dekker[9] found that emission of zone-boundary and optical phonons is the dominant scatter-

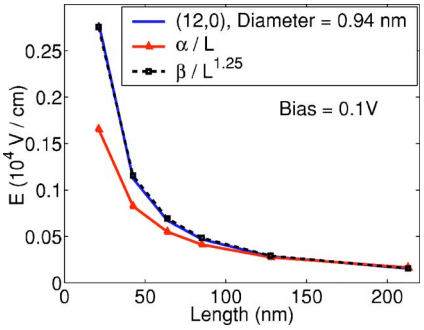


FIG. 6. (Color online) This plot shows the electric field at the midpoint versus nanotube length. A (12,0) nanotube at an applied bias of 100 mV is considered. The electric field decreases approximately as $L^{-1.25}$.

ing mechanism. The potential profiles at high bias for 42.6- and 213-nm-long (12,0) nanotubes are shown in Fig. 7. Due to the increased resistivity of the tube, the potential profile drops almost uniformly across the entire nanotube, which is qualitatively different compared to the low-bias (and no scattering) results of Fig. 4. The potential drop at the edges of the nanotube accounts for only 30% of the applied bias. Because a bias drops in the bulk of the tube at the expense of the edges, the potential drop at the edges also decreases with increase of nanotube length, falling to 15% for the longer nanotube. Due to the diameter dependence of the scattering rates, the (12,0) tube is 20 times more resistive than (240,0), with a mean free path of 5 nm for (12,0) versus 100 nm for (240,0). As a result, contrary to the low-bias case, the potential profiles for larger-diameter tubes show a larger voltage drop at the edges (inset of Fig. 7).

A major consequence of different potential profiles is the diameter dependence of the electric field at the nanotube center. In the ballistic limit, the electric field increases with diameter. However, the onset of diameter-dependent electron-phonon scattering at high bias makes the electric field decrease with diameter. This interesting reversal in electric field, demonstrated in Fig. 8, is rationalized by noting that

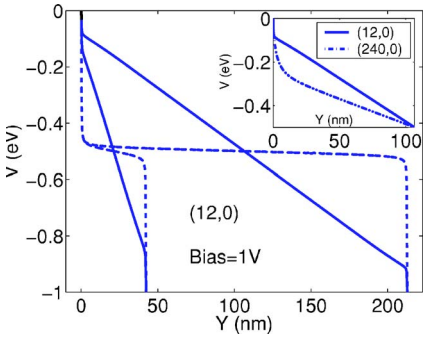


FIG. 7. (Color online) The potential as a function of position is shown for (12,0) nanotubes of lengths 42.6 and 213 nm (solid line). Shown for comparison is the potential profile in the ballistic case (dashed line). Inset: potential versus position for two different diameters. Note that contrary to the low-bias case, the electric field away from the edges is larger for smaller-diameter tubes. The lengths of the nanotubes are both 213 nm.

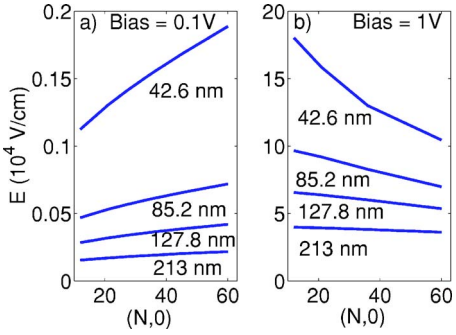


FIG. 8. (Color online) Electric field as a function of diameter for nanotubes of lengths 42.6, 85.2, 127.8, and 213 nm. (a) At low bias, a higher density of states per atom in smaller-diameter tubes leads to better screening (lower field). (b) At high bias, the trend is reversed and the electric field decreases with nanotube diameter.

the potential drop in the (12,0) nanotube has become almost linear because the mean free path is much smaller than the nanotube length, unlike in the (240,0) nanotube.

So far, the electrostatics of nanotubes under applied bias was discussed. We now compare the potential profiles in the ballistic limit and with scattering, in a nonzero electric field but at equilibrium. We choose an external electric field corresponding to a 1V bias but the Fermi levels of the source and drain contacts are set to −0.5 V. The electrostatic potential profiles in the two cases are almost identical as shown in Fig. 9 in sharp contrast to the nonequilibrium case. The reason is that, at equilibrium, following the Thomas-Fermi model, the potential profile should depend only on the DOS at the Fermi energy, which is unaffected by electron-phonon scattering.

We now discuss the current-voltage characteristics of small- and large-diameter nanotubes. For the (12,0) nanotube, only two crossing subbands contribute to transport. The ballistic current increases linearly with applied bias and the differential conductance is $4e^2/h$. Scattering by inelastic phonons causes current saturation and a decrease of the differential conductance (Fig. 10). The family of current-voltage characteristics shows the transition from the ballistic

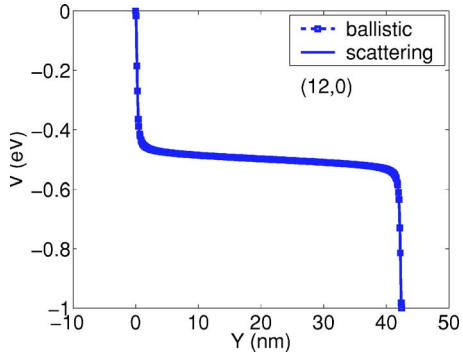


FIG. 9. (Color online) Potential profile of a nanotube at equilibrium but in the presence of an electric field corresponding to a bias of 1 V. The Fermi energy is −0.5 V throughout the tube. In contrast to the nonequilibrium case shown in Fig. 7, at equilibrium the potentials with and without scattering agree with each other. The electrostatic potential drop in the contact is neglected.

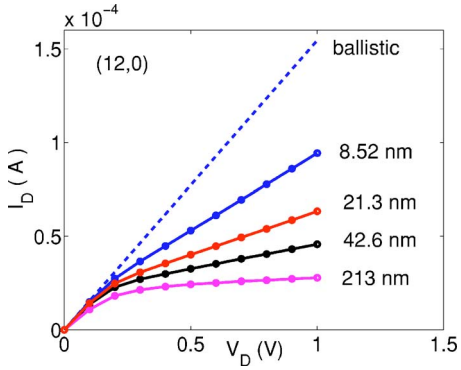


FIG. 10. (Color online) Current-voltage characteristics of a (12,0) nanotube of different lengths. The dashed line shows the ballistic limit. The resistivity of the tube increases with length, causing current saturation.

to the diffusive transport regime. The current saturation at the value of 25 μA for the longest tube agrees well with experimental data.

The current and differential conductance versus bias for a 42.6-nm nanotubes and a wide range of diameters are shown in Fig. 11. At low bias, phonon scattering is weak, so the current and conductance are still close to the ballistic limit. The saturation of current corresponds to the onset of inelastic phonon scattering and to the decrease of conductance at high

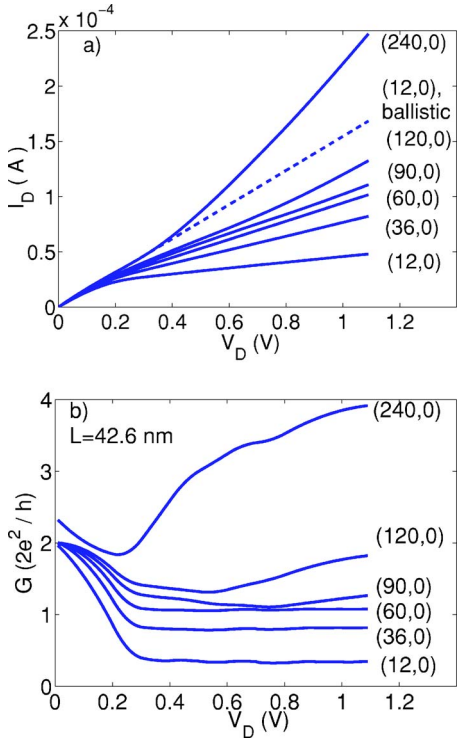


FIG. 11. (Color online) (a) Current-voltage characteristics of nanotubes of various diameters in the presence of electron-phonon scattering. (b) The differential conductance versus bias corresponding to (a). Inelastic phonon emission causes a decrease in the differential conductance at high bias. The contribution of noncrossing subbands leads to the increased low- and high-bias conductance for large-diameter tubes.

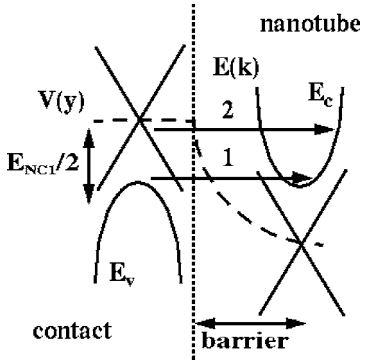


FIG. 12. Schematics for tunneling into noncrossing subbands at the source. The dashed line shows a potential profile $V(y)$, and the dotted line shows a boundary between a contact and a nanotube. Arrow 1 shows injection from a perfect contact with the band structure of a nanotube. Arrow 2 shows injection from end contacts with constant density of states or a scattering-assisted tunneling from crossing into noncrossing subbands.

bias. The differential conductance for small- and moderate-diameter nanotubes ($N=12$, 36, and 60) is qualitatively similar because of the same number of conducting modes. Quantitatively, the conductance increases with diameter due to decreasing scattering rates. This transition from the low- to high-bias regime is also present in large-diameter nanotubes ($N=90$, 120, and 240).

We note that the current increases with diameter. In the ballistic limit, the self-consistently calculated current of the (240,0) nanotube at 1 V is 310 μA and the differential conductance is almost $13e^2/h$. When scattering is included the current is decreased to 218.3 μA which is much larger than the current carried by a (12,0) nanotube of the same length, which is 45.7 μA. In addition, the differential conductance versus bias exhibits a qualitative change in shape. It is bell shaped for small-diameter nanotubes and transforms to a U shape for large-diameter nanotubes. As explained in Ref. 15, the increase of differential conductance with bias occurs due to *injection of electrons from contacts into the low-energy noncrossing subbands*. A schematics of the tunneling process is shown in Fig. 12: when the bias becomes larger than twice the band gap of the lowest noncrossing subband, electrons can tunnel from valence-band states $[E<-E_{NC1}/2+V(y)]$ in the source to conduction-band states $[E>E_{NC1}/2+V(y)]$ in the middle of the tube (the channel) and also from valence-band states in the channel to the conduction-band states in the drain. The lowest noncrossing subbands ($q=N/3-1$) in (90,0), (120,0) and (240,0) in the ballistic limit have band gaps $E_{NC1}=331$, 249, and 125 meV, respectively, and start to contribute to the current at biases of twice these values. Another useful quantity is the number of conducting channels: at $V_D=1$ V the number of subbands contributing to current in $(N,0)$ nanotube is {2, 2, 4, 6, 8, 16} for $N=\{12,36,60,90,120,240\}$. We note that the above picture is based on the assumption that the applied voltage drops symmetrically across the nanotube. In the case when one contact is much more resistive than the other and the applied voltage drops completely at one of the edges, the threshold for Zener tunneling is reduced, starting at biases equal to E_{NC1} rather

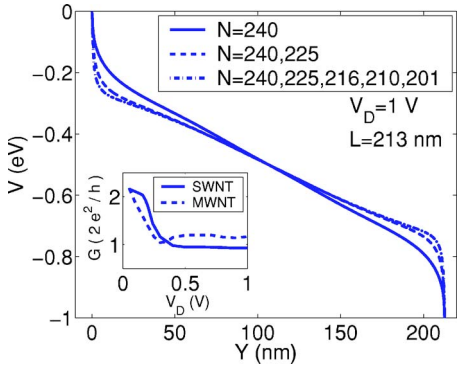


FIG. 13. (Color online) The potential profile in a single-walled and multiwalled NT. The barrier width in the outer (240,0) shell decreases due to the additional screening provided by the inner shells. Inset: a comparison of the differential conductance in single-walled (240,0) (dashed line) and multiwalled nanotubes of the same diameter. Both curves are bell shaped, signifying a quenching of Zener tunneling.

than $2E_{NC1}$. The number of conducting channels becomes {2, 6, 8, 12, 16, 32}. Additionally, if the contacts are metallic (and not perfect nanotube contacts), then the threshold bias for tunneling into noncrossing subbands will be further reduced by a factor of 2, an issue that will be discussed in Sec. III D. In addition to Zener tunneling between states with the same quantum number q, scattering also induces a phonon-assisted tunneling from crossing into noncrossing. Although these processes require intersubband scattering, the threshold bias is twice as low.

Another important feature of the differential conductance occurs at zero bias in the (240,0) nanotube (Fig. 11). The zero-bias conductance of the (240,0) nanotube is larger than $4e^2/h$ because the noncrossing subbands are partially filled and contribute to the current: the first noncrossing subband opens at an energy of 2.5 kT from the band center. This contribution is a simple intraband transport, determined by the population of the conduction band in the source and valence band in the drain, but rather insensitive to the details of the potential profile. At slightly higher biases the noncrossing subband contribution to current saturates to a constant value and the contribution to differential conductance decreases to zero, while the total conductance decreases to $4e^2/h$.

Increasing the length of a nanotube eventually makes the nanotube length larger than the mean free path. The current carried by a 213-nm-long (240,0) nanotube is now 86.6 μA at 1 V. Note that the differential conductance of a long nanotube shown in the inset of Fig. 13 has changed to bell shaped, in contrast to the short-nanotube case presented in Fig. 11. This is because when the nanotube length is many times the mean free path, the potential drop in the nanotube bulk becomes more linear, and as a result the barrier width (Fig. 12) for tunneling into noncrossing subbands increases. The noncrossing subbands then do not carry significant current. Overall, the voltage drop at the edges is a crucial factor determining the current contribution due to noncrossing subbands. It is directly related to the height and width of the barrier for tunneling into noncrossing subbands (Fig. 12), which depends on the scattering rate, nanotube length, and screening capability.

In the rest of the paper we discuss the role of electrostatic coupling to inner shells of a large-diameter nanotube and the role of contacts. Specifically, we will see that both issues lead to increased tunneling into noncrossing subbands because they lead to a decrease in barrier thickness.

C. Electrostatic gating due to inner shells

In multiwalled nanotubes (MWNT's) current flows only through the outermost shell as the inner shells are not electronically coupled to the metal leads[13] and intershell hopping is negligible.[23] Here, we are interested in the role of electrostatic coupling between the inner and outer shells in affecting the potential profile and current carried by the outer shell. We find that the inner shells effectively decrease the barrier width for tunneling into noncrossing subbands by providing additional screening. Figure 13 shows the potential profile in the outermost (240,0) shell. The inner shells are chosen to be metallic nanotubes with chirality indices $N=225$, 216, 210, and 201, such that a separation between the walls is roughly 3 Å. Even when just one metallic shell (225, 0) is added, the barrier width for tunneling into the first noncrossing subband decreases dramatically from 2.97 to 0.97 nm. Adding more shells further reduces the barrier width by smaller amounts, and the effect saturates. The differential conductance with the inner shells is qualitatively different as shown for the 213-nm-long (240,0) nanotube in the inset of Fig. 13. We find that the differential conductance at higher biases is larger but does not show an increase with bias when inner shells are included.

D. Influence of contact quality

We have so far assumed that the contacts are perfect—i.e., made of semi-infinite carbon nanotube leads. As mentioned in the Introduction, this physically corresponds to carbon nanotubes weakly coupled to the metal in which they are buried. So injection of electrons into the carbon nanotube lying between the contacts occurs from the carbon nanotube buried in the metal. As a result of this, injection into noncrossing subbands from the contact cannot occur at $E=0$. Note that selection rules do not permit injection of electrons from the crossing subband of the nanotube contact into noncrossing subbands between the contacts. In this section, we relax this condition and consider injection from the source contact into all nanotube subbands. The drain contact continues to be a nanotube contact. To accomplish this in a phenomenological manner, we model the contact self-energies in Eq. (10) as

$$\Sigma_{S,q}^{R} = -i\alpha\rho t_q^2, \tag{24}$$

where t_q is the original hopping parameter in Eq. (10), α is called the quality factor of the contacts, and ρ is the density of states of the contact which is chosen to be close to that of gold, $\rho=0.17$ eV^{-1}. The self-energy in Eq. (24) permits injection into the first noncrossing subband at a bias of E_{NC1} rather than the $2E_{NC1}$ with nanotube contacts.

We now present results for the potential profiles with good ($\alpha=1$) and poor ($\alpha=10^{-3}$ and $\alpha=10^{3}$) contacts in Fig.

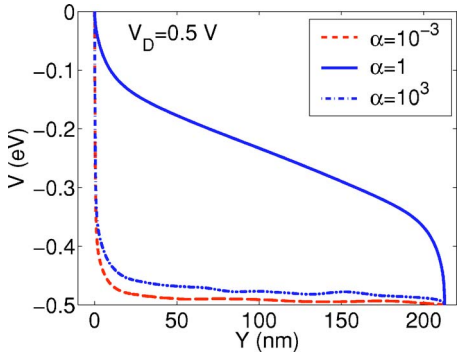


FIG. 14. (Color online) Potential profile for good ($\alpha=1$) and poor ($\alpha=10^{-3}$ and $\alpha=10^{3}$) source contacts. When the coupling is poor, voltage drops mostly at the source, which opens Zener tunneling for higher subbands.

14. Note that the terminology of poor and good contacts is relative to the intrinsic resistance of the nanotube that arises due to electron-phonon scattering. For $\alpha=1$, the potential profile of a (240,0) nanotube of length 213 nm is more or less symmetric and qualitatively similar to the perfect contact results presented in Fig. 13. For $\alpha=10^{-3}$ and $\alpha=10^{3}$, the electrostatic potential drops predominantly at the source end due to the large source-end contact resistance. The large potential drop and hence extremely thin barrier in the source end will facilitate tunneling into the noncrossing subbands for poor contact. As mentioned before, the asymmetry of the potential profile further reduces the threshold for tunneling to biases of $E_{NC1}/2$. The difference between the potential profiles for good and poor contacts has a profound influence on the shape of the differential conductance versus bias as shown in Fig. 15. For good contacts, the 213-nm-long nanotube shows a decreasing conductance with bias, in agreement with the perfect contact case. In contrast to this, for poor contacts, the differential conductance increases with bias. This increase with bias is a direct consequence of the potential profile shown by the dashed line in Fig. 14, which facilitates significant injection into noncrossing subbands. To see more directly that the noncrossing subbands are important in carrying current in long nanotubes with poor contacts, we calculate the current carried at a drain bias of 0.5 V as a function of the quality factor of the contacts with only crossing subbands and with all subbands. For good contacts, the current with only crossing subbands is very close to the current with all subbands (Fig. 16). But for poor contacts, the current with all subbands is significantly higher than the current with only crossing subbands. For example, when $\alpha=10^{-3}$, the current with all subbands is nearly an order of magnitude larger than with only crossing subbands. From Fig. 16 one can also see that the U-shaped differential conductance curve versus bias should be observed in a wide range of α except a small region near $\alpha\sim 1$, where noncrossing subbands do not carry significant current.

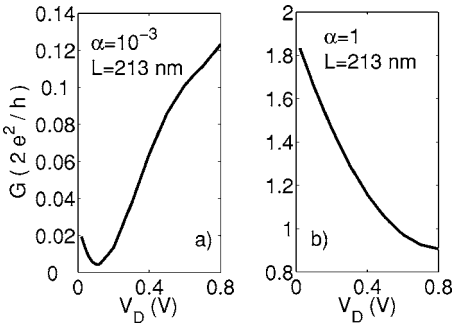


FIG. 15. Differential conductance G vs voltage V_D for (a) poor ($\alpha=10^{-3}$) and (b) good ($\alpha=1$) source contacts. The presence of tunneling into noncrossing subbands at $\alpha=10^{-3}$ qualitatively changes the G-V characteristics.

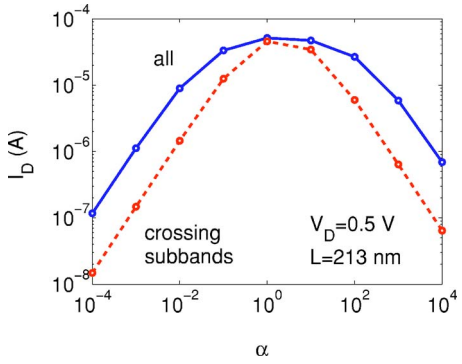


FIG. 16. (Color online) Current as a function of a source contact quality factor α. When the contact is poor (far from 1), the effect of higher subbands becomes important which signifies the increasing trend of differential conductance versus bias.

IV. CONCLUSION

We have studied transport in nanotubes of varying diameters and length, with electron-phonon scattering included. We find that charge self-consistency and the proper treatment of subband renormalization due to scattering are crucial in determining the correct current-voltage characteristics in large-diameter metallic nanotubes. In the small-bias ballistic limit, while the applied bias drops predominantly at the nanotube-contact interfaces, screening is incomplete at the tube center. Further, screening improves with a decrease in nanotube diameter due to the increased density of states per atom near the Fermi energy. At biases larger than 150 mV, electron-phonon scattering becomes important and the electrostatic potential drops primarily in the bulk of the nanotube rather than at nanotube-contact interfaces. However, as the mean free path for electron-phonon scattering increases with an increase in nanotube diameter, the potential drop in the bulk of the nanotube is larger for small-diameter nanotubes. As a result, the electric field at the nanotube center increases with an increase in diameter at small biases and decreases with an increase in diameter at high biases. This interesting reversal in electric field versus diameter is computationally seen for nanotube lengths from 42 to 213 nm. Overall, we find that larger-diameter nanotubes are capable of carrying more current because of an increase in mean free path with an increase in diameter and a lower-bias threshold for injection into noncrossing subbands. For small-diameter nanotubes of length 42 nm, we find that the differential conduc-

tance versus bias is bell shaped, with the largest value at zero bias. The reason for the smaller differential conductance at larger bias is reflection of electrons due to inelastic phonon scattering and the availability of only crossing subbands for charge transport. In contrast, large-diameter nanotubes of the same length show an increase in differential conductance with an increase in bias due to injection into noncrossing subbands and larger mean free paths. At a nanotube length (213 nm) longer than the mean free path, we find that the differential conductance for large-diameter nanotubes transitions to a bell-shaped curve similar to the small diameter case when coupling to contacts is good (small contact resistance). We have also modeled the role of inner shells in affecting the potential profile of the outer shell of a multiwalled nanotube. Here, we find that the inner shells cause a change in the electrostatic potential profile of the outer shell so as to make the potential drop sharper at the nanotube-contact interfaces. Our computational study has shown that the potential drop and differential conductance in metallic nanotubes is determined by an interesting interplay of diameter, mean free path, nature of contacts, and bias threshold for tunneling into noncrossing subbands. Finally, the most important result of this paper is that *the quality of contacts is the primary factor in determining the shape of the differential conductance versus bias in large-diameter nanotubes*. When the resistance at the nanotube-contact interface is larger than the intrinsic resistance of the nanotube, there is a large potential drop at the interface. The potential drop facilitates considerable tunneling into noncrossing subbands, and as a result the differential conductance of the 213 nm-long (240,0) nanotube with poor contact increases with bias, in contrast to the case with good contacts. This finding gives a possible explanation to the increase in differential conductance with bias seen in the recent experiments of Ref. 1, 2, 12, and 13.

ACKNOWLEDGMENTS

The calculations were performed at the facilities of NASA Advanced Supercomputing Division. We would like to thank Avik Ghosh for discussions on the density of states of gold.

*Electronic address: svizhenk@nas.nasa.gov
†Electronic address: anant@mail.arc.nasa.gov

[1] S. Frank, P. Poncharal, Z. L. Wang, and W. A. de Heer, Science **280**, 1744 (1998).
[2] P. Poncharal, S. Frank, Z. L. Wang, and W. A. de Heer, Eur. Phys. J. D **9**, 77 (1999).
[3] P. J. de Pablo, E. Graugnard, B. Walsh, R. P. Andres, S. Datta, and R. Reifenberger, Appl. Phys. Lett. **74**, 323 (1999).
[4] J. Nygard, D. H. Cobden, M. Bockrath, P. L. McEuen, and P. E. Lindelof, Appl. Phys. A: Mater. Sci. Process. **69**, 297 (1999).
[5] J. Kong, E. Yenilmez, T. W. Tombler, W. Kim, H. Dai, R. B. Laughlin, L. Liu, C. S. Jayanthi, and S. Y. Wu, Phys. Rev. Lett. **87**, 106801 (2001).
[6] F. Kreupl, A. P. Graham, G. S. Duesberg, W. Steinhogl, M. Liebau, E. Unger, and W. Honlein, Microelectron. Eng. **64**, 399 (2002).
[7] Q. Ngo, D. Petranovic, S. Krishnan, A. M. Cassell, Q. Ye, J. Li, M. Meyyappan, and C. Y. Yang, IEEE Trans. Nanotechnol. **3**, 311 (2004).
[8] B. Q. Wei, R. Vajtai, and P. M. Ajayan, Appl. Phys. Lett. **79**, 1172 (2001).
[9] Z. Yao, C. L. Kane, and C. Dekker, Phys. Rev. Lett. **84**, 2941 (2000).
[10] P. G. Collins, M. Hersam, M. Arnold, R. Martel, and Ph. Avouris, Phys. Rev. Lett. **86**, 3128 (2001).
[11] P. J. de Pablo, C. Gómez-Navarro, J. Colchero, P. A. Serena, J. Gómez-Herrero, and A. M. Baró, Phys. Rev. Lett. **88**, 036804 (2002).
[12] P. Poncharal, C. Berger, Y. Yi, Z. L. Wang, and W. A. de Heer, J. Phys. Chem. B **106**, 12104 (2002).
[13] Y. X. Liang, Q. H. Li, and T. H. Wang, Appl. Phys. Lett. **84**, 3379 (2004).
[14] M. P. Anantram, Phys. Rev. B **62**, R4837 (2000).
[15] A. Svizhenko, M. P. Anantram, and T. R. Govindan, IEEE Trans. Nanotech. (to be published), cond-mat/0504004.
[16] S. J. Tans, M. Devoret, H. Dai, A. Thess, R. E. Smalley, L. J. Geerligs, and C. Dekker, Nature (London) **386**, 474 (1997).
[17] M. P. Anantram, Appl. Phys. Lett. **78**, 2055 (2001).
[18] S. Datta, *Electronic Transport in Mesoscopic Systems* (Cambridge University Press, Cambridge, England, 1997).
[19] A. Svizhenko, M. P. Anantram, T. R. Govindan, B. Biegel, and R. Venugopal, J. Appl. Phys. **91**, 2343 (2002).
[20] J. Park, S. Rosenblatt, Y. Yaish, V. Sazonova, H. Ustunel, S. Braig, T. A. Arias, P. W. Brouwer, and P. L. McEuen, Nano Lett. **4**, 517 (2004).
[21] G. Pennington and N. Goldsman, Phys. Rev. B **68**, 045426 (2003).
[22] A. Svizhenko and M. P. Anantram, IEEE Trans. Electron Devices **50**, 1459 (2003).
[23] B. Bourlon, C. Miko, L. Forro, D. C. Glattli, and A. Bachtold, Phys. Rev. Lett. **93**, 176806 (2004).